Case study

Pore-scale simulation of miscible displacement in porous media using the lattice Boltzmann method

Ming Xia [a,b]

[a] Hunan Key Laboratory of Geomechanics and Engineering Safety, Xiangtan University, Xiangtan 411105, China
[b] College of Civil Engineering and Mechanics, Xiangtan University, Xiangtan 411105, China

ABSTRACT

A numerical model based on the lattice Boltzmann method is presented to investigate the viscous fingering phenomena of miscible displacement processes in porous media, which involves the fluid flow, heat transfer and mass transport. Especially, temperature- and concentration-dependent pore-fluid viscosity is considered. A complete list is derived and given for the conversion of relevant physical variables to lattice units to facilitate the understanding and implementation of the coupled problems involving fluid flow, heat transfer and mass transport using the LBM. To demonstrate the proposed model capacity, two different complex geometry microstructures using high resolution micro-computed tomography (micro-CT) images of core sample have been obtained and incorporated as computation geometries for modeling miscible displacement processes in porous media. The viscous fingering phenomena of miscible displacement processes are simulated in two different cases, namely in a channel and a porous medium respectively. Some influencing factors on the miscible displacement process, such as the pore-scale microstructure, Le number and Re number, are studied in great detail. The related simulation results have demonstrated that: (1) the existence of the pore-scale microstructure can have a significant effect on the front morphologies and front propagation speed in the miscible displacement process; (2) as the Le number increases, the fluid front and thermal front evolve differently, with the thermal front being less unstable due to more diffusion; (3) a larger Re number can lead to an increase in the propagation speed of the front.

© 2015 Elsevier Ltd. All rights reserved.

1. Introduction

The fingering instability is a general phenomenon in natural, which has a wide scientific and engineering background in the fields of geosciences, petroleum engineering, underground mining engineering, environment engineering and so forth. Generally, the fingering instability can be triggered by many mechanisms, such as viscosity mismatch between a less viscous fluid (i.e. displaced fluid) and a more viscous fluid (i.e. displacing fluid), variation of permeability and porosity in the porous media, and dissolved of trapped nonaqueous phase liquids (NAPL) into aqueous phase fluid. It is often called the viscous fingering instability (Ghesmat and Azaiez, 2009; Saffman and Taylor, 1958), chemical-dissolution front instability (Chadam et al., 1986; Zhao et al., 2008), and NAPL-dissolution front instability (Imhoff and Miller, 1996; Zhao et al., 2010), respectively. Owning to significant mechanism differences between them, this paper focuses on the consideration of viscous fingering problems.

In the case of viscous fingering instability, a less viscous fluid is intruded into a more viscous fluid, so that the interface between them can become unstable, resulting in the formation of viscous fingering. It should be noted that when injected fluid velocity is larger enough, the solid matrix will be destructed, and then the permeability will be increased. It is so-called hydraulic fracturing. Meanwhile, fluid-injection induced microseismicity will be generated, and its location can be analytical determined (Dong and Li, 2012; Dong et al., 2015a, 2015b). From the perspective of the two fluids interaction, viscous fingering instability may occur in two different processes (Homsy, 1987). One is the immiscible displacement, in which the surface tension at the interface cannot be neglected. The other is the miscible displacement, in which the surface tension at the interface can be neglected. The main focus of this investigation is on the computational aspects of the viscous fingering in the miscible displacement process. Thus, a large amount of researches have been carried out for understanding the viscous fingering phenomenon over the past decades (Islam and Azaiez, 2010; Rakotomalala et al., 1997; Yortsos and Zeybek, 1988). All these researches were conducted at the representative

elementary volume (REV) scale, in which fluid flow is often described by the Darcy's law. However, some flows deviated from the linear relationship between Darcy velocity and pressure gradient, which is called non-Darcy flow. Recently, Wang et al. (2012, 2013, 2015) have conductive some researches on the non-Darcy effects on the performance of coal seam gas wells. At the REV scale, a real porous medium, which contains the solid skeleton and the voids with fully or partly occupied by fluid, is averaged into a homogeneous medium by the macroscopic average method. The complex interaction between the fluid and microscopic porous structure in the porous medium at the REV scale are represented by two macroscopic physical quantities, namely porosity and permeability. Although this treatment has simplified and favored the theoretical analysis and numerical modeling, a detailed description of the pore structure is often neglected. Since pore structure may have an important effect on the miscible displacement, it is necessary to use a finer-scale model, in which the pore structure is directly considered, so that the characteristic of fluid flow can be described by the Navier–Stokes (NS) equations.

The accurate analytic solution of the miscible displacement process in porous media is a challenging problem due to the complexity of transport mechanisms with consideration of solid–fluid interaction and the difficulty in representing the complicated and tortuous nature of a porous medium accurately. As an alternative approach, numerical modeling has become a useful tool for investigating the viscous fingering in miscible displacement problems through solving the NS equations directly. However, from the macroscopic point of view, the major difficulty in modeling the viscous fingering of miscible displacement in the porous medium is the description of the complex geometry structure at the pore-scale with some continuum-based numerical methods, such as the finite element method (FEM) and finite difference method (FDM). On the contrary, the lattice Boltzmann method (LBM) is a mesoscopic simulation method, and the complex geometries of the porous media can be easily considered. In particular, the LBM has a sound theoretical foundation, on which the incompressible NS equations can be derived form the Boltzmann equation through the Chapman–Enskog procedure (He and Luo, 1997). This method has already been used to study both the miscible and immiscible displacement (Dong et al., 2011; Kang et al., 2004), in which the fluid flow and mass transport were considered. Although the previous works considered the displacement in a channel or a porous medium with regular pore structure, both the real pore structure and heat transfer process are neglected.

The forthcoming contents of this paper are arranged as follows. In Section 2, the coupled lattice Boltzmann model that can be used to simulate the coupled fluid flow, heat transfer and mass transport problem is described. In Sections 3 and 4, the miscible displacement process in both a channel and a porous medium are simulated, respectively. The temperature- and concentration-dependent pore-fluid viscosity and the effect of the pore-structure are taken into account. In addition, to demonstrate the proposed model capacity, two different complex geometry microstructures using high resolution micro-computed tomography (micro-CT) images of core sample have been obtained and incorporated as computation geometries for modeling miscible displacement processes in porous media. Finally, some conclusions and discussion drawn from this study are given in Section 5.

2. The coupled lattice Boltzmann model

2.1. Lattice Boltzmann model for coupled fluid flow, heat transfer and mass transport

In the LBM, a space domain is divided into regular lattice nodes,

while a fluid domain is divided into a large number of fluid particles that are allowed to move between lattice nodes or stay at rest. At the same time, a time domain is also divided into a large number of discrete time steps. During each discrete time step of the simulation, there are two main processes for each fluid particle, namely the collision process and the streaming process. In the collision process, a fluid particle can collide with another fluid particle that arrives at the same node. The macroscopic variables in this node are updated by following some rules. While in the streaming process, the updated fluid node can move to its neighboring lattice node along the moving direction. Within these processes, data exchange between neighboring nodes is only necessary.

According to the Boussinesq approximation, fluid density can be assumed to be a linear function of both temperature and concentration, which is expressed as follows:

$$\rho = \rho_0 \big[1 - \beta_T (T - T_0) - \beta_C (C - C_0) \big] \tag{1}$$

where ρ is the pore-fluid density; ρ_0 is the reference density of pore-fluid; T is the pore-fluid temperature; T_0 is the reference pore-fluid temperature; C is the chemical species concentration; C_0 is the reference concentration of the chemical species; β_T is the thermal expansion coefficient of pore-fluid; β_C is the concentration expansion coefficient of the chemical species.

The considered coupled problem involves fluid flow, heat transfer and mass transport in a two dimensional system with the temperature- and concentration-dependent fluid densities. The corresponding governing equations of the problem can be expressed as follows:

$$\frac{\partial \rho}{\partial t} + \nabla \cdot (\rho \mathbf{u}) = 0 \tag{2}$$

$$\frac{\partial (\rho \mathbf{u})}{\partial t} + \nabla \cdot (\rho \mathbf{u} \mathbf{u}) = -\nabla p + \nabla^2 (\rho v \mathbf{u}) + \rho \mathbf{F} \tag{3}$$

$$\frac{\partial T}{\partial t} + \nabla \cdot (\mathbf{u} T) = \alpha \nabla^2 T \tag{4}$$

$$\frac{\partial C}{\partial t} + \nabla \cdot (\mathbf{u} C) = D \nabla^2 C \tag{5}$$

$$\mathbf{F} = g \beta_T (T - T_0) \mathbf{j} + g \beta_C (C - C_0) \mathbf{j} \tag{6}$$

where $\mathbf{u} = (u_x, u_y)$ is the velocity vector; p is the pore-fluid pressure; v is the kinematical viscosity; $\mathbf{F}$ is the body force; α is the thermal diffusion coefficient; D is the mass diffusion coefficient; g is the gravity acceleration component in the vertical direction.

Based on the idea of the LBGK model, the temperature and concentration can be treated as passive scalars (Chen and Doolen, 1998). Thus, fluid velocity, temperature and chemical species concentration can be treated individually. By following the popular linearized single-relaxation-time BGK formulation, the density-, temperature- and concentration-distribution functions at each time step are given as follows:

$$f_i(\mathbf{x} + \mathbf{e}_i \Delta t, t + \Delta t) = f_i(\mathbf{x}, t)$$
$$- \frac{\Delta t}{\tau_f} \big[f_i(\mathbf{x}, t) - f_i^{eq}(\mathbf{x}, t) \big]$$
$$+ \Delta t F_i \ (i = 0, \ldots \ldots, \ 8) \tag{7}$$

$$g_i(\mathbf{x} + \mathbf{e}_i\Delta t, t + \Delta t) = g_i(\mathbf{x}, t) - \frac{\Delta t}{\tau_T}\Big[g_i(\mathbf{x}, t) - g_i^{eq}(\mathbf{x}, t)\Big] \ (i = 0, \ldots\ldots, \ 8) \tag{8}$$

$$h_i(\mathbf{x} + \mathbf{e}_i\Delta t, t + \Delta t) = h_i(\mathbf{x}, t) - \frac{\Delta t}{\tau_C}\Big[h_i(\mathbf{x}, t) - h_i^{eq}(\mathbf{x}, t)\Big] \ (i = 0, \ldots\ldots, \ 8) \tag{9}$$

$$F_i = \frac{\omega_i \rho \mathbf{F} \cdot \mathbf{e}_{iy}}{c_s^2} \tag{10}$$

where for any grid node $\mathbf{x}$, $\mathbf{x} + \mathbf{e}_i\Delta t$ is its nearest neighboring node along direction i; f_i^{eq}, g_i^{eq} and h_i^{eq} are the equilibrium density-, temperature- and concentration-distribution functions, respectively; τ_f, τ_T and τ_C are the dimensionless relaxation time of the density, temperature and concentration, respectively; c_s is the lattice sound speed; $\mathbf{e}_i$ are the discrete velocities; Δt is the discrete time step; ω_i is the weighting factor.

Note that Eqs. (7–10) can be recovered from Eqs. (2–6), which is the theoretical foundation for the success of the coupled lattice Boltzmann model for modeling fluid flow, heat transfer and mass transport problems.

In the commonly used D2Q9 model, the fluid particle at each node can move to its eight immediate neighboring nodes with discrete velocities $\mathbf{e}_i$ ($i=0, \ldots, 8$). The discrete velocities are defined as follows:

$$\mathbf{e}_i = \begin{cases} (0, 0) & i = 0 \\ c\left(\cos\frac{(i-1)\pi}{2}, \ \sin\frac{(i-1)\pi}{2}\right) & i = 1, 2, 3, 4 \\ c\left(\cos\frac{(2i-9)\pi}{4}, \ \sin\frac{(2i-9)\pi}{4}\right) & i = 5, 6, 7, 8 \end{cases} \tag{11}$$

where $c (= h/\Delta t)$ is the lattice speed with h and Δt being the lattice spacing and time step, respectively.

The equilibrium density-, temperature- and concentration-distribution functions depend only on the fluid density and velocity, which are defined in the D2Q9 model as follows:

$$f_i^{eq} = \omega_i \rho\Big[1 + \frac{3}{c^2}\mathbf{e}_i\cdot\mathbf{u} + \frac{9}{2c^4}(\mathbf{e}_i\cdot\mathbf{u})^2 - \frac{3}{2c^2}\mathbf{u}\cdot\mathbf{u}\Big] \ (i = 0, \ldots\ldots, \ 8) \tag{12}$$

$$g_i^{eq} = \omega_i T\Big[1 + \frac{3}{c^2}\mathbf{e}_i\cdot\mathbf{u}\Big] \ (i = 0, \ldots\ldots, \ 8) \tag{13}$$

$$h_i^{eq} = \omega_i C\Big[1 + \frac{3}{c^2}\mathbf{e}_i\cdot\mathbf{u}\Big] \ (i = 0, \ldots\ldots, \ 8) \tag{14}$$

where ω_i is the weighting factor with $\omega_0 = 4/9$, $\omega_{1-4} = 1/9$ and $\omega_{5-8} = 1/36$.

The macroscopic fluid variables, namely density, velocity, temperature and chemical species concentration, can be recovered from the distribution functions as follows:

$$\rho = \sum_{i=0}^{8} f_i \tag{15}$$

$$\rho\mathbf{u} = \sum_{i=0}^{8} f_i\mathbf{e}_i \tag{16}$$

$$T = \sum_{i=0}^{8} g_i \tag{17}$$

$$C = \sum_{i=0}^{8} h_i \tag{18}$$

The fluid pressure field is determined by the following equation of state: $p = c_s^2\rho$, where c_s is termed the fluid speed of sound and is related to lattice speed c as follows: $c_s = c/\sqrt{3}$ in the D2Q9 model.

The kinematical viscosity, thermal diffusion coefficient, and mass diffusion coefficient of the fluid is implicitly determined as follows:

$$v = \frac{1}{3}(\tau_f - 0.5)\frac{h^2}{\Delta t} \tag{19}$$

$$\alpha = \frac{1}{3}(\tau_T - 0.5)\frac{h^2}{\Delta t} \tag{20}$$

$$D = \frac{1}{3}(\tau_C - 0.5)\frac{h^2}{\Delta t} \tag{21}$$

2.2. Concentration- and temperature-dependent fluid viscosity

The concentration- and temperature-dependent viscosity is implemented in the present study, which is expressed as follows (Tan and Homsy, 1986):

$$\mu(C, T) = \mu_2 exp(-\alpha_C C - \alpha_T T) \tag{22}$$

where μ_2 is the viscosity of displaced fluid; α_C is the natural logarithm of the viscosity ratio (i.e. $\alpha_C = \log(\mu_2/\mu_1)$); thermal mobility ratio α_T represents the natural logarithm of the ratio of the viscosity (μ_{T2}/μ_{T1}) at two different temperatures.

2.3. Boundary and initiation conditions

Fig. 1 shows the geometry and boundary conditions for the miscible displacement problem, in which the computational domain for this example is a rectangular box with the length of L_x and height of L_y. The pore space is initially fully-filled with a more viscous fluid, and then a less viscous fluid with an initial velocity
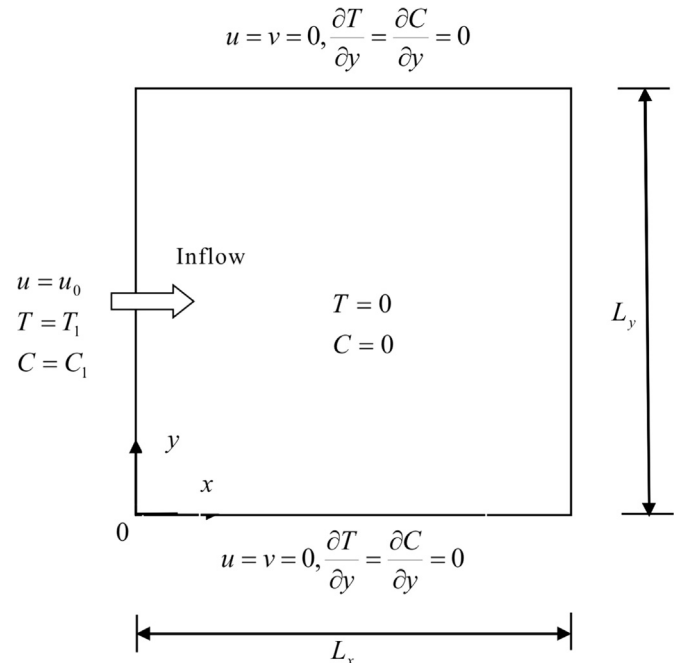

Fig. 1. Geometry and boundary conditions for the miscible displacement problem in a porous medium.

of u_0 is applied to the left boundary to displace the more viscous fluid, implying that there is a horizontal through flow from the left to the right of the computational domain in the miscible displacement process. Due to the viscosity difference between the displaced fluid and displacing fluid, the interface between them will become unstable, and then the viscous fingering will be generated. Both the temperature of the displaced fluid and the concentration of the chemical species are equal to zero initially. While the temperature of the displacing fluid applied to the left boundary of the computation domain is T_l. Similarly, the concentration of the chemical species applied to the left boundary of the computation domain is C_l.

The treatments of boundary conditions play an important role within both the FEM and LBM. However, compared with the FEM, the boundary condition cannot be directly defined in the LBM. All these macroscopic parameters at the boundary condition should be converted into its corresponding distribution function at the boundary nodes. In the present study, since the pore-structures are considered, the treatment of solid–fluid interface in the solid surface is a very important issue. The half-way bounce-back boundary condition is adopted to represent no-slip conditions along the solid surface. It can be defined that the nodes covered by the solid particles are solid nodes, while the nodes in the fluid region are fluid nodes. Note that the wall boundary is assumed to be situated halfway between a solid and fluid node so as to achieve second-order accuracy (Feng et al., 2007). The half-way bounce-back rule requires that the incoming fluid particles from the fluid node be reflected and bounced back in the opposite direction, i.e. $f_{i'}(\mathbf{x}_f, t + \Delta t) = f_i(\mathbf{x}_f, t)$, where $\mathbf{x}_f$ is the position of the fluid node close to the wall, i is the streaming direction that points at the wall, and i' is the opposite direction.

While in the present study, the temperature and concentration boundary scheme is imposed on the inlet and outlet. Regarding the outlet, the open flow boundary condition is adopted. The upper and lower boundary adopted the no-slip boundary condition. Some concentration boundary conditions have been developed (Chen et al., 2013; Zhang et al., 2012). In the present study, the approach of Chen et al. (2013) is adopted at the computational domain boundary. Meanwhile, the solid skeleton is impermeable. Thus, as for the thermal and mass boundary conditions at the fluid–solid interface, the bounce-back wall boundary condition is also adopted. The lattice units are used to speed up the computation.

It should be noted that when the lattice nodes are located on the solid sub-domains, the density-, temperature- and concentration-distribution functions in Eqs. (7)–(9) are all equal to zero, and hence the fluid velocity, fluid temperature and chemical species concentration need not be calculated. The reason for this is that the pore structure is impermeable, and then the fluid flow only through the pore space at the pore scale. Recently, the complicated fluid behavior in fractured porous media with variable permeable pore structure is simulated at the REV scale (Gao and Xing, 2012; Gao et al., 2014).

2.4. Conversion between physical and lattice units

It should be noted that both the physical units and the lattice units can be used in the LBM formulation and computation. However, compared with the physical units, the formulation associated with the lattice units is simpler and computational more efficient. This is the reason why the lattice units system is widely adopted in the LBM formulation and computation. In the present work, the LBM is also implemented using the lattice units with necessary conversions between the physical and lattice Boltzmann systems. In order to facilitate the implementation and gain a better understanding of the LBM, a theoretical analysis to established the

relationship of the variables used in the LB model between these two unit systems has been conducted, in which a superscript 'p' and 'LB' are used to indicate a variable in the physical units and lattice units, respectively.

The relationship of physical and lattice units associated with temperature and chemical species concentration can be expressed as follows:

$$T^{LB} = \frac{T^p - T^p_{\min}}{T^p_{\max} - T^p_{\min}} \tag{23}$$

$$C^{LB} = \frac{C^p - C^p_{\min}}{C^p_{\max} - C^p_{\min}} \tag{24}$$

where T^p and T^{LB} are the temperatures in the physical system and lattice system, respectively; $T^p_{\min}$ and $T^p_{\max}$ are the minimum and maximum temperatures in the physical system, respectively; C^p and C^{LB} are the concentrations of the chemical species in the physical system and lattice system, respectively; $C^p_{\min}$ and $C^p_{\max}$ are the minimum and maximum concentrations of the chemical species in the physical system, respectively.

According to Eq. (1), the following equations exist:

$$\rho^p = \rho^p_0(1 - \beta^p_T \Delta T^p - \beta^p_C \Delta C^p) \tag{25}$$

$$\rho^{LB} = \rho^{LB}_0(1 - \beta^{LB}_T \Delta T^{LB} - \beta^{LB}_C \Delta C^{LB}) \tag{26}$$

$$\rho^p = \rho_0 \rho^{LB} \tag{27}$$

$$\rho^p_0 = \rho_0 \rho^{LB}_0 \tag{28}$$

Substituting Eqs. (27) and (28) into Eqs. (25) and (26) yield the following equations:

$$\beta^p_T \Delta T^p = \beta^{LB}_T \Delta T^{LB} \tag{29}$$

$$\beta^p_C \Delta C^p = \beta^{LB}_C \Delta C^{LB} \tag{30}$$

Substituting Eqs. (23) and (24) into Eqs. (29) and (30) yield the following equations:

$$\beta^p_T = \frac{1}{T^p_{\max} - T^p_{\min}} \beta^{LB}_T \tag{31}$$

$$\beta^p_C = \frac{1}{C^p_{\max} - C^p_{\min}} \beta^{LB}_C \tag{32}$$

The relationship between physical system and lattice system associated with other nine variables (i.e. L, u, g, c_s, v, k, ϕ, α, D) in the coupled problems involving fluid flow, heat transfer and mass transport using the LBM can be analytically determined using the dimensional analysis. These parameters can be divided into independent and dependent parameters. According to the Buckingham π theorem (Buckingham, 1914), two independent dimensions associated with two of the nine parameters need to be used for describing the coupled problems involving fluid flow, heat transfer and mass transport using the LBM, so that seven dimensionless parameters (i.e. $g/(u^2/L)$, c_s/u, v/Lu, k/L^2, ϕ, α/Lu, D/Lu) are involved in the mathematical expressions of the coupled problems. According to the dimensional analysis (Tan, 2011), the following equations exist:

$$\frac{g^p}{\left[\frac{(u^p)^2}{L^p}\right]} = \frac{g^{LB}}{\left[\frac{(u^{LB})^2}{L^{LB}}\right]} \tag{33}$$

$$\frac{c_s^p}{u^p} = \frac{c_s^{LB}}{u^{LB}} \tag{34}$$

$$\frac{v^p}{L^p u^p} = \frac{v^{LB}}{L^{LB} u^{LB}} \tag{35}$$

$$\frac{k^p}{(L^p)^2} = \frac{k^{LB}}{(L^{LB})^2} \tag{36}$$

$$\text{ø}^p = \text{ø}^{LB} \tag{37}$$

$$\frac{\alpha^p}{L^p u^p} = \frac{\alpha^{LB}}{L^{LB} u^{LB}} \tag{38}$$

$$\frac{D^p}{L^p u^p} = \frac{D^{LB}}{L^{LB} u^{LB}} \tag{39}$$

As for the conversion between physical and lattice units, the following equations exist (He et al., 2009):

$$L^p = L_r L^{LB} \tag{40}$$

$$\mathbf{u}^p = u_r \mathbf{u}^{LB} \tag{41}$$

where L_r is the reference length, m; u_r is the reference velocity, m/s.

After substituting Eqs. (40) and (41) into Eqs. (33)–(39), a complete list is given in Table 1 for the conversion of the variables used in the LBM between these two unit systems.

3. Simulation of viscous fingering phenomenon of miscible displacement in a channel

In order to model the viscous fingering phenomenon of miscible displacement, especially involving the coupled fluid flow, heat transfer and mass transport with the consideration of temperature- and concentration-dependent viscosity, the proposed

Table 1
Conversion between physical and lattice units.

Variable	Physical	Lattice	Relationship
Density	ρ^p	ρ^{LB}	$\rho^p = \rho_0 \rho^{LB}$
Length	L^p	L^{LB}	$L^p = L_r L^{LB}$
Velocity	$\mathbf{u}^p$	$\mathbf{u}^{LB}$	$\mathbf{u}^p = u_r \mathbf{u}^{LB}$
Spacing	$h^p = L_r$	$h^{LB} = 1$	–
Discrete time step	$\Delta t^p = \frac{L_r}{u_r}$	$\Delta t^{LB} = 1$	–
Gravity acceleration	$\mathbf{g}^p$	$\mathbf{g}^{LB}$	$\mathbf{g}^p = \frac{(u_r)^2}{L_r} \mathbf{g}^{LB}$
Sound speed	c_s^p	c_s^{LB}	$c_s^p = u_r c_s^{LB}$
Kinematic viscosity	ν^p	ν^{LB}	$\nu^p = L_r u_r \nu^{LB}$
Permeability	k^p	k^{LB}	$k^p = (L_r)^2 k^{LB}$
Porosity	ø^p	ø^{LB}	$\text{ø}^p = \text{ø}^{LB}$
Temperature	T^p	T^{LB}	$T^{LB} = \frac{T^p - T_{\min}^p}{T_{\max}^p - T_{\min}^p}$
Chemical species concentration	C^p	C^{LB}	$C^{LB} = \frac{C^p - C_{\min}^p}{C_{\max}^p - C_{\min}^p}$
Thermal expansion coefficient of pore-fluid	β_T^p	β_T^{LB}	$\beta_T^p = \frac{1}{T_{\max}^p - T_{\min}^p} \beta_T^{LB}$
Concentration expansion coefficient of the chemical species	β_C^p	β_C^{LB}	$\beta_C^p = \frac{1}{C_{\max}^p - C_{\min}^p} \beta_C^{LB}$
Thermal diffusion coefficient	α^p	α^{LB}	$\alpha^p = L_r u_r \alpha^{LB}$
Mass diffusion coefficient	D^p	D^{LB}	$D^p = L_r u_r D^{LB}$

coupled lattice Boltzmann model is designed to simulate the viscous fingering phenomenon of miscible displacement in a channel firstly. Since the real pore structure may have certain effects on the viscous fingering of the miscible displacement at the pore-scale, the porous medium is considered through a detailed parametric study in the next section. In the simulations, the computational domain is divided into a 400×100 lattice grid. The following properties of the fluid are used in the LB models: the injection velocity (u_0) at the inlet is 0.02, the viscosity of the displaced fluid (v_2) is 0.02 with a solute mobility ratio $\alpha_C = 1.6$, the thermal diffusion coefficient (α) is 0.0056, the mass diffusion coefficient (D) is 0.0056. The temperature and chemical species concentration are both equal to 1.0 at the left boundary. In the following sections, only the considered parameter is changed, while keeping other parameters unchanged. In the numerical simulation, the average density and the initial density of the fluid are all equal to 1.0, while the particle speed is 1.0.

3.1. Effect of Le number

In order to investigate the effect of the *Le* number ($Le = \alpha/D$) on the evolution of the miscible displacement process in a channel, two different *Le* numbers are presented. In this section, the case simply corresponds to a displacement with a solute mobility ratio $\alpha_C = 1.6$ where heat transfer has no effect on viscosity (i.e. $\alpha_T = 0.0$). The mass diffusion coefficient (D) is fixed to 0.0056, while the thermal diffusion coefficient (α) is choose to 0.0056, 0.056, and 0.56, respectively, so that the corresponding *Le* number is 1, 10, and 100, respectively. All other parameters are kept the same as those used in Section 2.3.

Fig. 2 shows the comparison of the miscible displacement process with different *Le* numbers at $t=20,000$. It is interesting to note that the fluid front and thermal front evolve at the same rate with $Le=1$. The reason for this is that the heat transfer and mass transport processes have the same diffusion coefficients. For all values of the *Le* number, finger instability phenomenon of the same pattern is observed in the concentration field. This indicates that the *Le* number has little effect on the concentration field. On the contrary, it has great effect on the temperature field. Furthermore, as the *Le* number increases, the fluid front and the thermal front evolve differently, with the fluid front being more unstable. The reduction in instability on the thermal front is due to the enhancement of the thermal dispersion in such flow. The temperature field becomes more diffuse with a weakly front without major finger. Especially for $Le=100$, the thermal front appears to be stable.

3.2. Effect of Re number

The general expression for the *Re* number is given as follows: $\text{Re} = u_0 L_y/v_1$, where u_0 and v_1 is the injection velocity and viscosity of the displacing fluid, respectively. In order to investigate the effect of the *Re* number on the evolution of the miscible displacement process in a channel, several simulations with different *Re* numbers are performed by changing the initial velocity of the displacing fluid. Four different injection velocities of the displacing fluid, namely 0.004, 0.008, 0.02 and 0.04, are considered. The corresponding *Re* numbers are 100, 200, 500 and 1000, respectively. In this section, mobility ratio is fixed with $\alpha_C = 1.6$, $\alpha_T = 0.0$.

Fig. 3 shows the effects of *Re* number on the evolution of the miscible displacement process in a channel. It can be observed that the evolution pattern of the miscible displacement process has the similar characteristic, for which the viscous fingering can be observed as time goes on. At the early stage ($t=2000$), the interfaces are slightly bent and no finger is formed when $Re=100$. However, when $Re=500$, two tips in the lower and upper part of
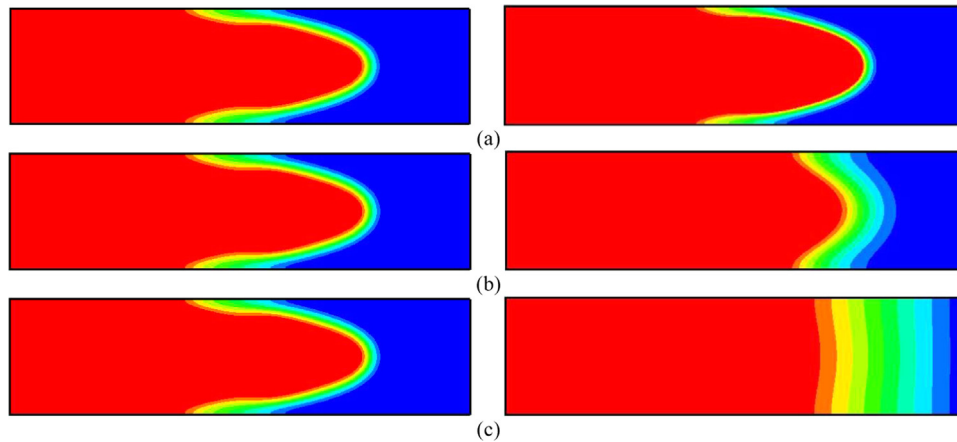
Fig. 2. Effects of the *Le* number on the miscible displacement process in a channel: (a) *Le*=1; (b) *Le*=10 and (c) *Le*=100. The left part is the chemical species concentration distributions, while the right part is the temperature distributions.

interface have formed in a symmetric manner. At $t=10000$, the finger is formed in both cases. At $t=20000$, the finger is also formed in both cases, but the patterns are totally different. For instance, the interface tip is located at $x=110.1$ when $Re=100$, while the interface tip is located at $x=320.4$ when $Re=500$. This means that a larger Re number will enhance the evolution of miscible displacement, resulting in early breakthrough and reduced sweeping efficiency. In general, the breakthrough time is shorted for a larger Re number. It is obvious that the Re number has a great influence on the evolution pattern and the breakthrough time of the miscible displacement. From the oil recovery engineering point of view, this should be avoided to obtain a higher economic benefit.

In order to quantitatively compare the difference, the transverse-averaged concentration of chemical species and the concentration of chemical species at the middle height of the model along the flow direction (i.e. $y = L_y/2$) are shown in Fig. 4. The transverse-averaged concentration of chemical species is defined as follows (Rakotomalala et al., 1997):

$$\bar{C}(x, t) = \frac{1}{L_y} \int_0^{L_y} C(x, y, t)dy \tag{42}$$

As shown in Fig. 4(a), the transverse-averaged concentration of chemical species due to different Re numbers has the same behavior. At the area near the inlet, the transverse-averaged concentration of chemical species is equal to the chemical species

concentration of the displacing fluid. It decreases along the flow direction gradually. Meanwhile, the larger the Re number is, the width the interface has (i.e. longer the finger length has). It can be seen from Fig. 4(b) that the interface fronts have a general behavior, indicating that behind the interface front, the concentration of the chemical species is equal to the concentration of the chemical species in the displacing fluid, while before it, the concentration of the chemical species is equal to the concentration of the chemical species in the displaced fluid. As for the concentration between them, a sharpness of the interface can be observed. On the other hand, an increase of the Re number in the miscible displacement system can lead to an increase in the propagation speed of the viscous interface front.

4. Simulation of viscous fingering phenomenon of miscible displacement in a porous medium

After the miscible displacement process in a channel is simulated, it can be used to simulate the same kind of problem in a porous medium. Convergence of the numerical results has also been tested by simulating this case at lattice systems of 100×100, 200×200, and 400×400. As similar evolution processes have been observed in the later two cases, a lattice system of 200×200 with a porous structure in Fig. 5 was used in the subsequent numerical study. While the modeling parameters, boundary and initiation conditions are the
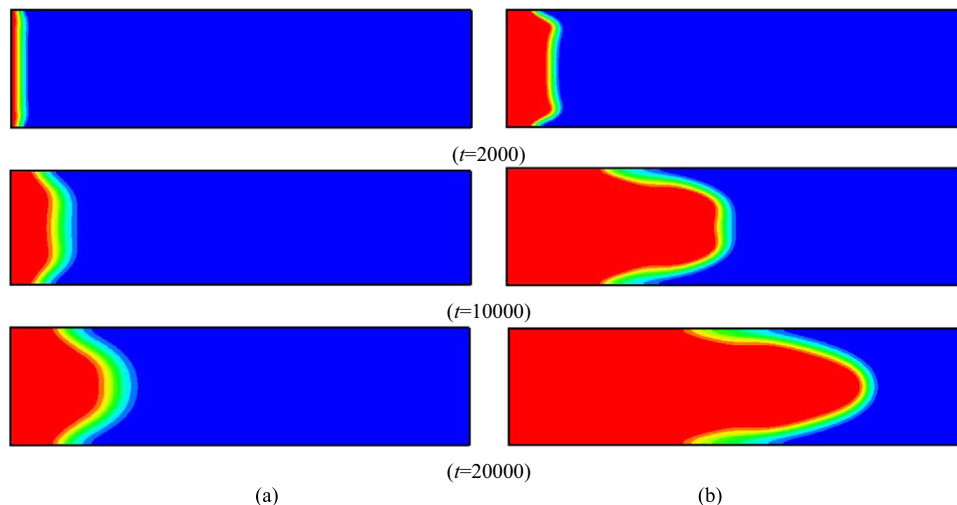

Fig. 3. Effects of the *Re* number on the miscible displacement process in a channel at different time instants: (a) *Re*=100 and (b) *Re*=500.
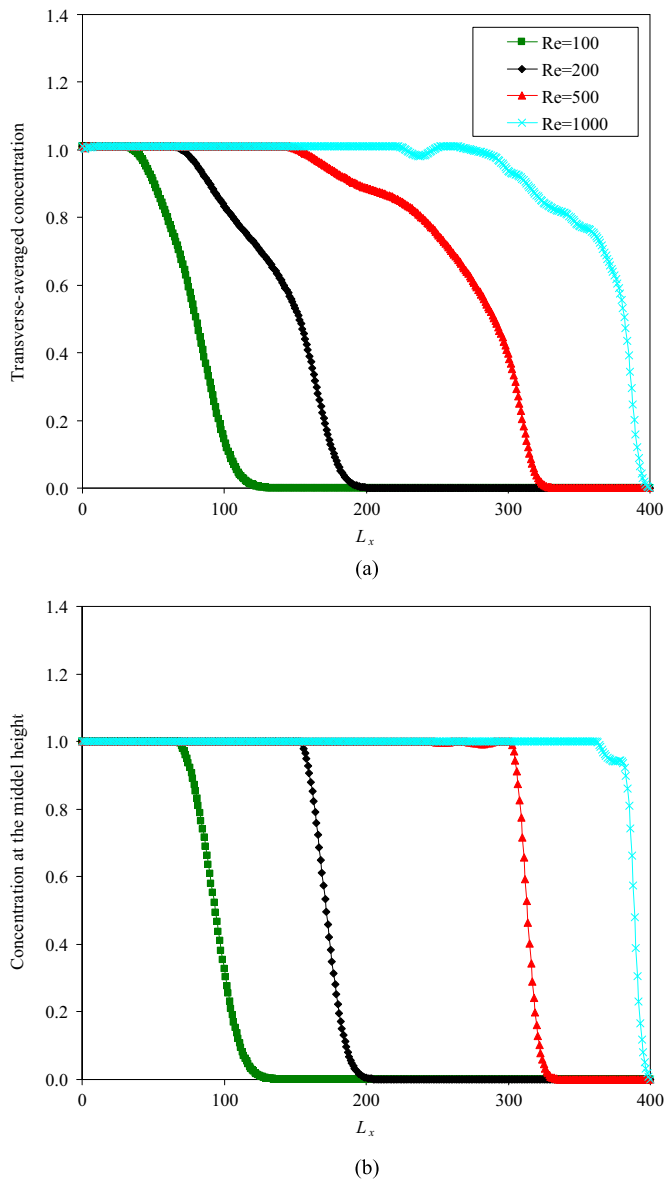
Fig. 4. Effects of the Re numbers on the chemical species concentration at t=20,000: (a) transverse-averaged concentration and (b) concentration at the middle height.
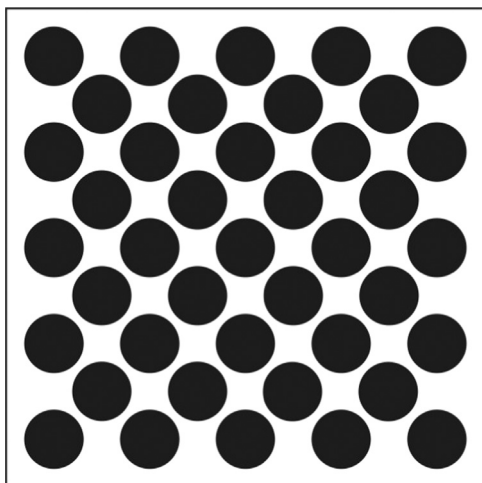

Fig. 5. The pore-scale microstructure in the porous medium.

same as those used in a channel except that a regular porous medium is considered. Meanwhile, solute mobility $\alpha_C = 1.6$, and thermal mobility ratio $\alpha_T = 1.0$ are used in the simulation.

4.1. Effect of pore-scale structure

As stated in the Introduction, most of the previous studies involving both immiscible and miscible displacement in the porous medium do not consider the real pore structure, which may have a certain effect on the miscible displacement process. With consideration of this point, the regular pore structure in the porous medium is represented by two different pore-scale microstructures in this section for simplicity. One is a regular solid skeleton, which contains 25 solid particles in an in-line arrangement manner, while the other one contains 41 solid particles in a staggered arrangement manner (see Fig. 5). Fig. 6 shows the effects of two pore-scale microstructures on the miscible displacement process in the porous medium. Generally, it can be seen that the existence of the solid skeleton have a significant effect on the viscous fingering front morphologies when the fluid passes through it. At the early stage of the miscible displacement, irregular fingers are formed within both pore-scale microstructures. On the other hand, the front pattern of the miscible displacement process in the porous medium with the in-line arrangement solid skeleton has a similar characteristic to that in a channel, indicating that the front pattern appears in a symmetrical manner. However, with the in-line arrangement of the solid skeleton, a big front is divided into six small bent fronts associated with little interaction among them. Furthermore, due to the staggered arrangement of the solid skeleton, there is a totally different front pattern in the porous medium. At the later stage of the miscible displacement, the interface front tip in the staggered arrangement porous medium is lag behind that in the regular porous medium. The reason for this is that the existing of the solid skeleton has prevented the fluid flow along the flow direction in a certain degree. It should be noted that the width of interface front is increasing as time goes in the later stage of the miscible displacement (Fig. 6 (b)). Meanwhile, the interface is less clearly. This means that the diffusion mechanism may be enlarged by the existence of the solid skeleton at the pore-scale in the miscible displacement.

On the other hand, it also indicates that when the pore-scale microstructure is considered, viscous fingering associated with the miscible displacement process in the porous medium is much more complicated and complex than in the channel. At the early stage of the miscible displacement, the interface is clear in both cases. However, in the later stage of the miscible displacement, the interface is complex. In some areas, the displacing fluid is surrounded by the displaced fluid. While in other areas, the displaced fluid is surrounded by the displacing fluid. It is clear that the homogeneous medium (i.e. the miscible displacement in a channel) does not have a significant effect on the viscous fingering pattern, as shown in Fig. 2. Although some researchers simulated miscible and/or immiscible displacement at pore-scale using the LBM, they mostly treated porous medium with a higher porosity, so that the viscous fingering can be formed at different times. However, such a treatment cannot simulate the fundamental mechanism of the miscible displacement processes associated with viscous fingering instability problem. To simulate the miscible displacement processes more realistically, the number of solids in the porous medium should be increase to match the actual porosity. This indicates that the detailed and real microstructure of a porous medium, which consists of a mixture of different material constituents and microscopic cracks, are required in the engineering analysis.

To demonstrate the model capacity, more complex microstructures should be considered. Based on high-resolution
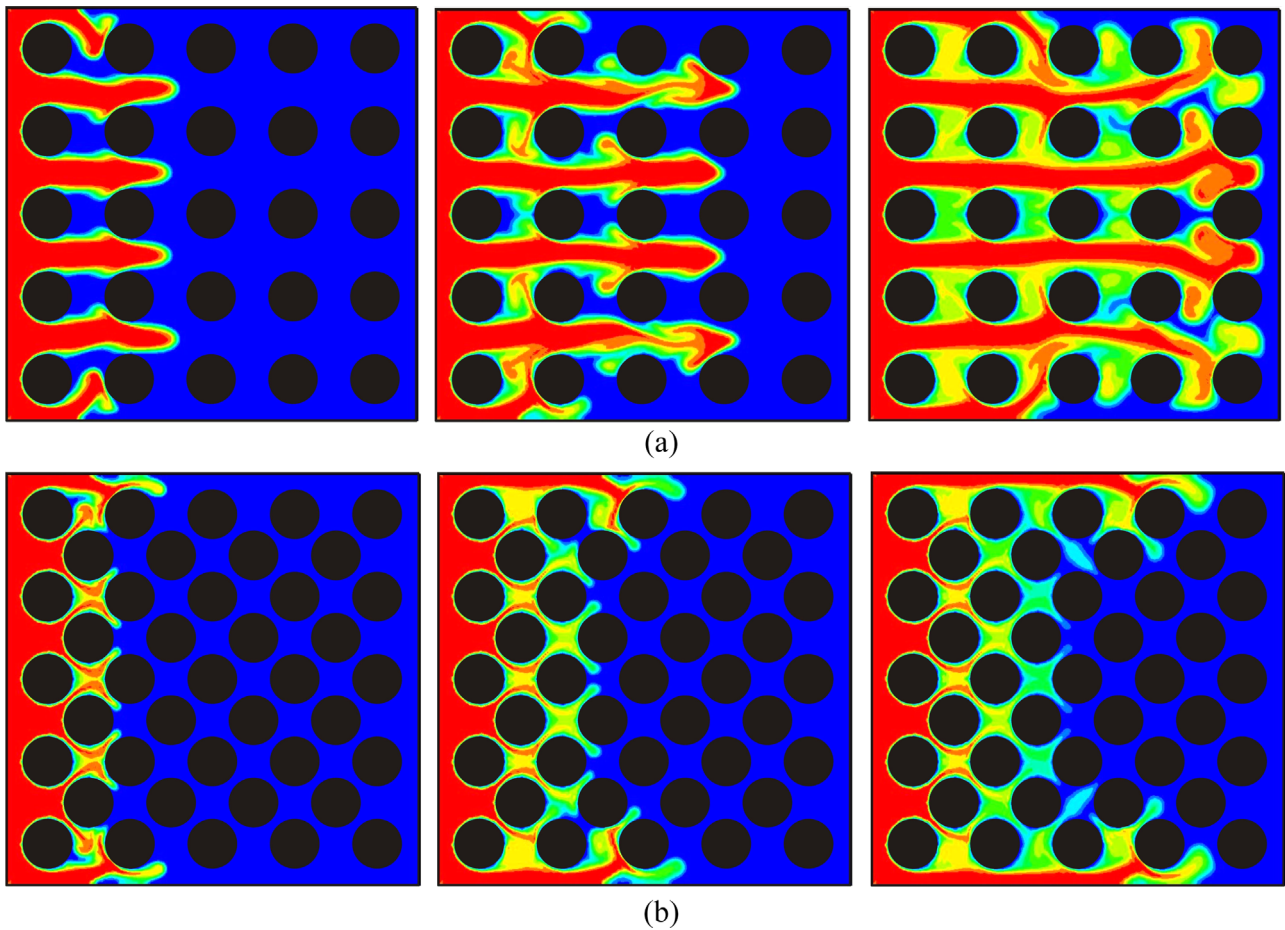
Fig. 6. Effects of the pore-scale microstructure on the miscible displacement process in a porous medium at $t=2000$, 4000 and 8000: (a) the in-line arrangement and (b) the staggered arrangement.
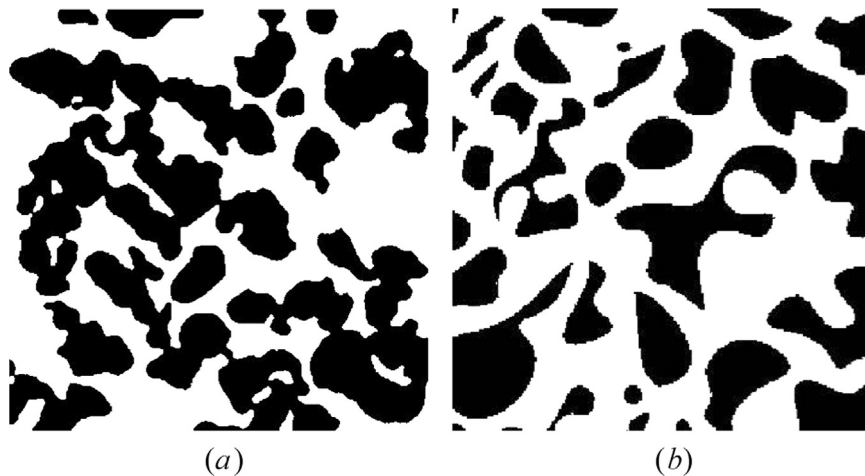

Fig. 7. Pore microstructures obtained after image processing of the micro-CT scan: (a) pore microstructure 1; (b) pore microstructure 2.

scanned digital images, the microstructures of rock sample can be measured by using the image processing technique. In this way, two pore-scale microstructures representing the porous media are extracted from the micro-computed tomography (micro-CT) images of core sample (Fig. 7), after noise reduction, binary conversion and simplification. Pore microstructure 1 is of 458×459 in resolution (Fig. 7(a)), while pore microstructure 2 is of 348×349 in resolution (Fig. 7(b)). In the Fig. 7, the black region represents solid matrix, while white region represents pore space. Form the Fig. 7, it can be seen that the pore-scale microstructures represent the

porous media is more complex and realistic, compared with Fig. 5. As the pore-scale microstructure is obtained, the solid matrix information (e.g. its coordinates of solid nodes) can be obtained through searching and then stored as an input file in a 2D array style. After that, there are converted to computational domains and incorporated as computation geometries for modeling miscible displacement processes.

Fig. 8 shows the miscible displacement process within two pore-scale microstructures of a realistic porous media. This further indicates that the displacement patterns in the porous medium
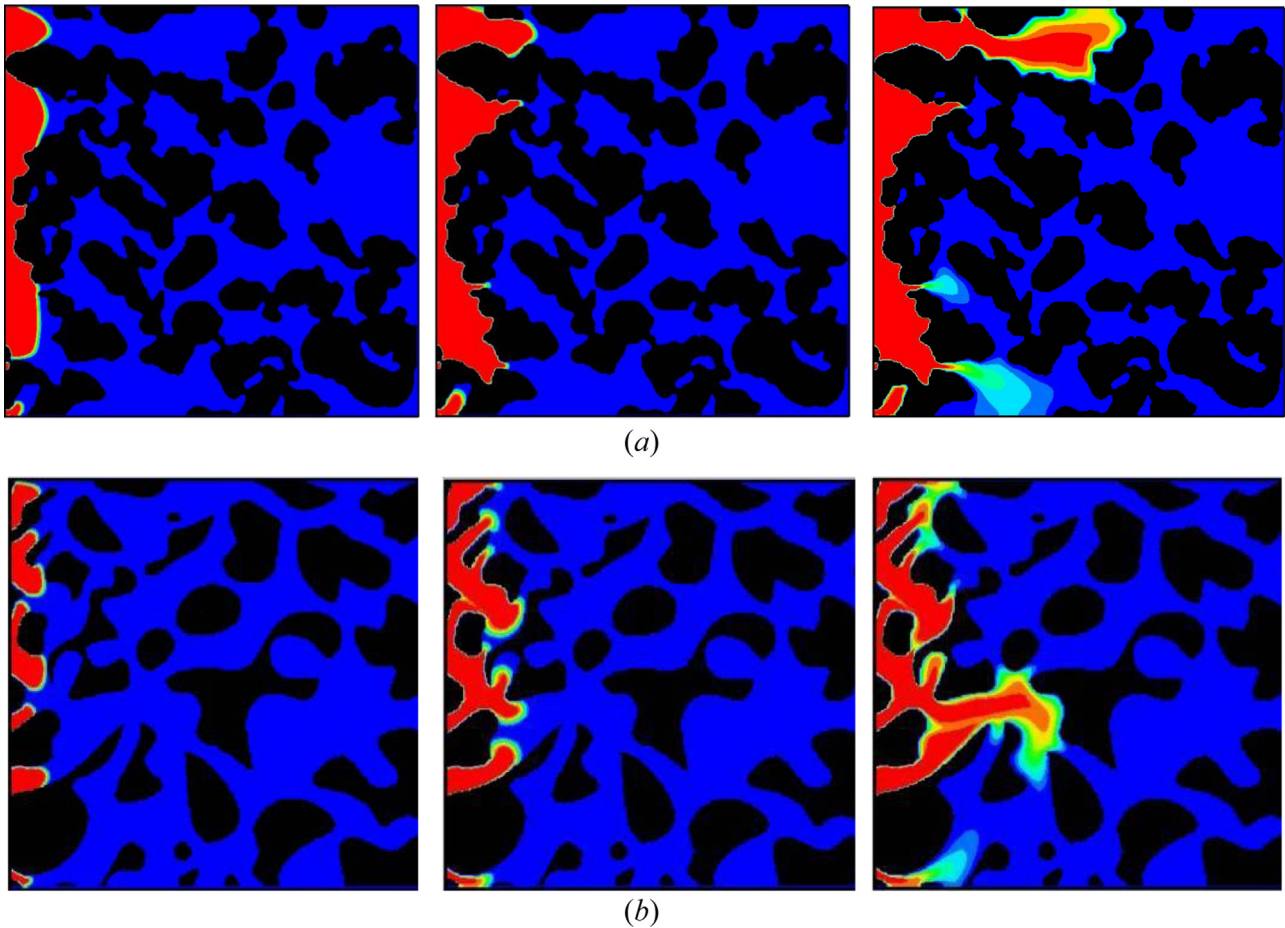
Fig. 8. The miscible displacement process in porous media with complex microstructures: (a) pore microstructure 1; (b) pore microstructure 2.

with complex geometry microstructure are significantly different from the displacement ones in a channel or a porous medium with regular geometry microstructure, implying that the present model can be used to simulate miscible displacement problem in the porous media with complex geometry microstructures at the pore-scale. These two application examples with the consideration of complex microstructure demonstrate the usefulness of the proposed model in investigate the miscible displacement processes in a realistic porous media with complex microstructures at the pore scale.

4.2. Effect of Re number

Further study is carried out on the effects of *Re* number on the miscible displacement process in a staggered porous medium. Keeping the other parameters unchanged, three different *Re* numbers, which are 675, 1350 and 2700, are considered. Fig. 9 shows the effects of *Re* number on the evolution of the miscible displacement process in a porous medium. It can be seen that the larger the *Re* number is, the quicker the viscous front of the interface propagates. For example, the front tip at the centre part reaches $x=60.1$, 83.5 and 115.4 at $t=10{,}000$, when $Re=675$, 1350
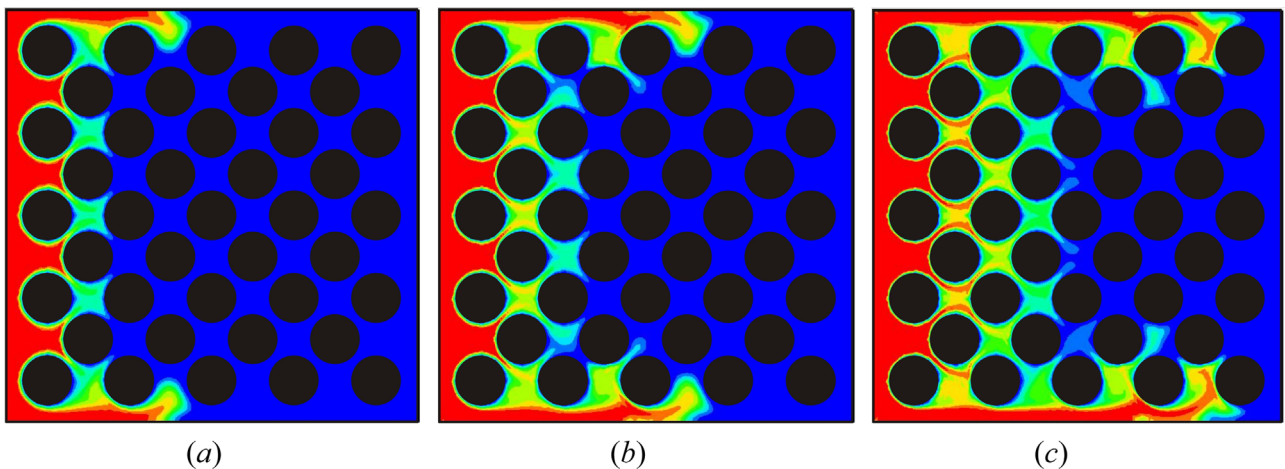

Fig. 9. Effects of the *Re* number on the miscible displacement process in a staggered arrangement porous medium at $t=10000$: (a) $Re=675$; (b) $Re=1350$ and (c) $Re=2700$.

and 2700, respectively. This behavior has the same characteristic as that in a channel (see Fig. 3). It should be noted that as the *Re* number increases, the width of the interface front, represented by the distance between the displacing fluid and the displaced fluid, is greater. It demonstrates that an increase of *Re* number can lead to a more diffusion interface front.

5. Discussion and conclusions

To simulate viscous fingering phenomena of the miscible displacement process in a porous medium at the pore-scale, a numerical model based on the lattice Boltzmann model involving fluid flow, heat transfer and mass transport is presented. In this model, the temperature- and concentration-dependent pore-fluid viscosities are considered. To demonstrate the proposed model capacity, two different complex geometry microstructures using high resolution micro-computed tomography (micro-CT) images of core sample have been obtained and incorporated as computation geometries for modeling miscible displacement processes in porous media. This model is used to simulate the miscible displacement in three different pore structures, namely a channel, a regular porous medium and a staggered arrangement porous medium. Some influencing factors on the miscible displacement process, such as the pore-scale microstructure, *Le* number and *Re* number, are studied in great detail. The related simulation results have demonstrated that: (1) the existence of the pore-scale microstructure can have a significant effect on the front morphologies and front propagation speed in the miscible displacement process; (2) as the *Le* number increases, the fluid front and the thermal front evolve differently, with the thermal front being less unstable due to more diffusion; (3) a larger *Re* number can lead to an increase in the propagation speed of the interface front.

The discrete element method (DEM) is a promising numerical tool for simulation problems of a discrete/discontinuous nature (Cundall and Strack, 1979), which can account for the particles interaction and transport. And then it has been extended to modeling mechanical deformation and heat conduction problems at the laboratory length-scale in the last 10–15 years (Potyondy and Cundall, 2004; Xia and Zhou, 2010; Xia et al., 2014; Xia and Zhao., 2014; Xia, 2015a; Zhao et al., 2012; Zhao, 2013). Furthermore, with the establishment of the upscale theory recently (Feng and Owen, 2014; Xia, 2015b), the DEM can be used to modeling mechanical deformation and heat conduction problems at both the engineering length-scale and geological length-scale directly. On the other hand, as mentioned in the Introduction, the LBM can be used to modeling the fluid flow problems. For this reason, the coupled DEM-LBM model is proposed to modeling the fluid–particle interaction problems at the pore-scale (Cook et al., 2004; Feng et al., 2007, 2010; Owen et al., 2011). Although both the coupled DEM-LBM model and the present proposed model can be used to modeling the fluid–particle interaction problems with complex boundary geometries at the pore scale, the coupled DEM-LBM approach is particularly advantageous when used to model fluid–particle interaction problems with moving boundaries. On the contrary, the present proposed model is particularly advantageous when used to modeling the fluid–particle interaction problems with stationary boundaries. Compared with the coupled DEM-LBM model, the present proposed model is easy to implement and computationally more efficient, from the computational point of view. In addition, not only can the present proposed model be used to deal with fluid flow problems, but also it can be used to deal with heat transfer and mass transport problems in the porous media with complex geometry microstructure at the pore-scale.

References

Buckingham, E., 1914. On physically similar systems: illustrations of the use of dimensional equations. Phys. Rev. 4 (4), 345–376.

Chadam, J., Hoff, D., Merino, E., Ortoleva, P., Sen, A., 1986. Reactive infiltration instabilities. IMA J. Appl. Math. 36, 207–221.

Chen, L., Kang, Q., Robinson, B.A., He, Y.L., Tao, W.Q., 2013. Pore-scale modeling of multiphase reactive transport with phase transitions and dissolution-precipitation processes in closed systems. Phys. Rev. E 87, 043306.

Chen, S., Doolen, G.D., 1998. Lattice Boltzmann method for fluid flows. Annu. Rev. Fluid Mech. 30, 329–364.

Cook, B.K., Noble, D.R., Williams, J.R., 2004. A direct simulation method for particle–fluid systems. Eng. Comput. 21, 151–168 2-4.

Cundall, P.A., Strack, O.D.L., 1979. A discrete numerical model for granular assemblies. Geotechnique 29 (1), 47–65.

Dong, B., Yan, Y.Y., Li, W.Z., 2011. LBM simulation of viscous fingering phenomenon in immiscible displacement of two fluids in porous media. Transp. Porous Media 88 (2), 293–314.

Dong, L., Li, X., 2012. Three-dimensional analytical solution of acoustic emission or microseismic source location under cube monitoring network. Trans. Nonferrous Met. Soc. China 22 (12), 3087–3094.

Dong, L., Li, X., Zhou, Z., Chen, G., Ma, J., 2015a. Three-dimensional analytical solution of acoustic emission source location for cuboid monitoring network without pre-measured wave velocity. Trans. Nonferrous Met. Soc. China 25 (1), 293–302.

Dong, L., Wesseloo, J., Potvin, Y., Li, X., 2015b. Discrimination of mine seismic events and blasts using the Fisher Classifier, Naive Bayesian Classifier and logistic regression. Rock. Mech. Rock. Eng. 48, 1–29. http://dx.doi.org/10.1007/s00603-015-0733-y.

Feng, Y.T., Han, K., Owen, D.R.J., 2007. Coupled lattice Boltzmann method and discrete element modelling of particle transport in turbulent fluid flows: computational issues. Int. J. Numer. Methods Eng. 72 (9), 1111–1134.

Feng, Y.T., Han, K., Owen, D.R.J., 2010. Combined three-dimensional lattice Boltzmann method and discrete element method for modelling fluid–particle interactions with experimental assessment. Int. J. Numer. Methods Eng. 81 (2), 229–245.

Feng, Y.T., Owen, D.R.J., 2014. Discrete element modelling of large scale particle systems–I: exact scaling laws. Comput. Part. Mech. 1 (2), 159–168.

Gao, J., Xing, H., 2012. LBM simulation of fluid flow in fractured porous media with permeable matrix. Theor. Appl. Mech. Lett. 2 (3), 032001.

Gao, J., Xing, H., Tian, Z., Muhlhaus, H., 2014. Lattice Boltzmann modeling and evaluation of fluid flow in heterogeneous porous media involving multiple matrix constituents. Comput. Geosci. 62, 198–207.

Ghesmat, K., Azaiez, J., 2009. Miscible displacement of reactive and anisotropic dispersive flows in porous media. Transp. Porous Media 77, 489–506.

He, X., Luo, L.S., 1997. Lattice Boltzmann model for the incompressible Navier–Stokes equation. J. Stat. Phys. 88, 927–944 3-4.

He, Y.L., Wang, Y., Li, Q., 2009. Lattice Boltzmann Method: Theory and Applications. Science Press, Beijing.

Homsy, G.M., 1987. Viscous fingering in porous media. Annu. Rev. Fluid Mech. 19, 271–311.

Imhoff, P.T., Miller, C.T., 1996. Dissolution fingering during the solubilization of nonaqueous phase liquids in saturated porous media: 1. Model predictions. Water Resour. Res. 32, 1919–1928.

Islam, M.N., Azaiez, J., 2010. Miscible thermo-viscous fingering instability in porous media. Part 2: numerical simulations. Transp. Porous media 84 (3), 845–861.

Kang, Q., Zhang, D., Chen, S., 2004. Immiscible displacement in a channel: simulations of fingering in two dimensions. Adv. Water Resour. 27, 13–22.

Owen, D.R.J., Leonardi, C.R., Feng, Y.T., 2011. An efficient framework for fluid-structure interaction using the lattice Boltzmann method and immersed moving boundaries. Int. J. Numer. Methods Eng. 87, 66–95 1-5.

Potyondy, D.O., Cundall, P.A., 2004. A bonded-particle model for rock. Int. J. Rock. Mech. Min. Sci. 41 (8), 1329–1364.

Rakotomalala, N., Salin, D., Watzky, P., 1997. Miscible displacement between two parallel plates: BGK lattice gas simulations. J. Fluid Mech. 338, 277–297.

Saffman, P.G., Taylor, G., 1958. The penetration of a fluid into a porous medium or Hele–Shaw cell containing a more viscous liquid. Proc. R. Soc. Lond. Ser. A 245, 312–329.

Tan, C.T., Homsy, G.M., 1986. Stability of miscible displacements in porous media: rectilinear flow. Phys. Fluids 29 (11), 3549–3556.

Tan, Q.M., 2011. Dimensional Analysis with Case Studies in Mechanics. Springer-Verlag, Berlin.

Yortsos, Y.C., Zeybek, M., 1988. Dispersion driven instability in miscible displacement in porous media. Phys. Fluids 31 (12), 3511–3518.

Wang, J.G., Kabir, A., Liu, J., Chen, Z., 2012. Effects of non-Darcy flow on the performance of coal seam gas wells. Int. J. Coal Geol. 93, 62–74.

Wang, J.G., Liu, J., Kabir, A., 2013. Combined effects of directional compaction, non-Darcy flow and anisotropic swelling on coal seam gas extraction. Int. J. Coal Geol. 109, 1–14.

Wang, J.G., Ju, Y., Gao, F., Peng, Y., Gao, Y., 2015. Effect of CO_2 sorption-induced anisotropic swelling on caprock sealing efficiency. J. Clean. Prod. 103, 685–695.

Xia, M., Zhou, K., 2010. Particle simulation of the failure process of brittle rock under triaxial compression. Int. J. Miner., Metall. Mater. 17 (5), 507–513.

Xia, M., Zhao, C., 2014. Simulation of rock deformation and mechanical characteristics using clump parallel-bond models. J. Cent. South Univ. 21 (7), 2885–2893.

Xia, M., Zhao, C., Hobbs, B.E., 2014. Particle simulation of thermally-induced rock damage with consideration of temperature-dependent elastic modulus and strength. Comput. Geotech. 55, 461–473.

Xia, M., 2015a. Thermo-mechanical coupled particle model for rock. Trans. Nonferrous Met. Soc. China 25 (7), 2367–2379.

Xia, M., 2015b. An upscale theory of thermal-mechanical coupling particle simulation for non-isothermal problems in two-dimensional quasi-static system. Eng. Comput. 32 (7), 2136–2165.

Zhang, T., Shi, B., Guo, Z.L., Cai, Z., Lu, J., 2012. General bounce-back scheme for concentration boundary condition in the lattice-Boltzmann method. Phys. Rev. E 85, 016701.

Zhao, C., Hobbs, B.E., Hornby, P., Ord, A., Peng, S., Liu, L., 2008. Theoretical and numerical analyses of chemical-dissolution front instability in fluid-saturated porous rocks. Int. J. Numer. Anal. Methods Geomech. 32, 1107–1130.

Zhao, C., Hobbs, B.E., Ord, A., 2010. Theoretical analyses of nonaqueous-phase-liquid dissolution induced instability in two-dimensional fluid-saturated porous media. Int. J. Numer. Anal. Methods Geomech. 34, 1767–1796.

Zhao, Z., Jing, L., Neretnieks, I., 2012. Particle mechanics model for the effects of shear on solute retardation coefficient in rock fractures. Int. J. Rock. Mech. Min. Sci. 52, 92–102.

Zhao, Z., 2013. Gouge particle evolution in a rock fracture undergoing shear: a microscopic DEM study. Rock. Mech. Rock. Eng. 46 (6), 1461–1479.